https://doi.org/10.5194/egusphere-2025-6126
Preprint. Discussion started: 30 December 2025

Methane intensity and emissions across major oil and gas basins and individual jurisdictions using MethaneSAT observations

James P. Williams[1,2], Joshua Benmergui[1,2,3], Marvin Knapp[1,2,3], Mark Omara[1,2], Anthony Himmelberger[1,2], Ethan Kyzivat[3], Kaiya Weatherby[1,2], Ben Lyke[1,2], Jack Warren[1,2], Katlyn MacKay[1,2], Sasha Ayvazov[2], Marcus Russi[2], Nicholas LoFaso[2], Tom Melendez[2], Christopher C. Miller[1,2,3], Sebastien Roche[1,2,3], Maryann Sargent[3], Jonathan Franklin[3], Maya Nasr[3], Zhan Zhang[3], David Miller[3], Bingkun Luo[3], Luis Guanter[1,4], Steven P. Hamburg[1,2], Steven C. Wofsy[3], Ritesh Gautam[1,2]

[1]Environmental Defense Fund, New York, NY, USA 10010
[2]MethaneSAT, LLC, Austin, TX, USA 78701
[3]Harvard University, Cambridge, MA, USA 02138
[4]Research Institute of Water and Environmental Engineering (IIAMA), Universitat Politècnica de València, Valencia, Spain

Correspondence to: James P. Williams (jamwilliams@edf.org), Ritesh Gautam (rgautam@edf.org)

Abstract. Mitigating global anthropogenic methane emissions is widely recognized as an effective strategy to reduce near-term climate warming. Here, we use satellite observations from MethaneSAT (2024–2025) to characterize methane emissions from major oil and gas basins worldwide. MethaneSAT addresses a critical gap in access to quantitative measurements of spatially distributed area emissions, providing high-resolution (~4 km × 4 km), wide-swath (220–440 km) coverage. We analyze aggregated MethaneSAT emissions across six major oil and gas producing regions: the Permian (USA), San Joaquin (USA), Eagle Ford (USA/Mexico), Amu Darya (Turkmenistan and Uzbekistan), and the Zagros Foldbelt (Iran/Iraq). Regional oil and gas emissions span more than an order of magnitude, ranging from 408 t h^{-1} (95% CI: 303–516 t h^{-1}) for the Permian basin to 30 t h^{-1} (95% CI: 20.3–41.1 t h^{-1}) in the San Joaquin basin. Methane intensities also vary substantially across basins and sub-basins, with more than an order of magnitude variation in both production-normalized and energy-normalized metrics. These differences reflect diverse factors, including contrasts in oil versus gas production, infrastructure age, contributions of lower-producing wells, and presence or absence of emission mitigation practices. Across jurisdictions, including counties and districts, we find consistent underestimation by gridded EPA-GHGI and EDGAR bottom-up inventories relative to MethaneSAT-derived emissions. Overall, MethaneSAT data provide basin-wide and sub-regional insights into methane emissions and intensities, offering critical scientific and policy-relevant information to support targeted and effective methane mitigation strategies.

https://doi.org/10.5194/egusphere-2025-6126
Preprint. Discussion started: 30 December 2025

1 Introduction

Methane is a potent greenhouse gas and has been identified as a crucial target for emissions reduction to meet near-term climate change goals [1]. Due to the potency of methane as a greenhouse gas, more than 150 countries have pledged to reduce methane emissions as part of the Global Methane Pledge which was signed in 2021, with new actions introduced in the 29th United Nations Climate Change Conference in Azerbaijan held in 2024. Fortunately, several sectors responsible for significant portions of the anthropogenic methane budget offer attainable mitigation pathways with reductions being achievable with existing technology and/or updated industry practices [2]. A crucial component of reducing methane emissions is the ability to detect, quantify, and locate methane emissions over time, which in turn informs effective mitigation strategies.

Bottom-up methane inventories like the gridded Environmental Protection Agency Greenhouse Gas Inventory (gridded EPA-GHGI)[3] in the US and the Emissions Database for Global Atmospheric Research (EDGAR)[4] are both examples of spatially-explicit methane data sources used to track progress towards methane mitigation targets, but are limited by input data such as emission factors and activity data[5]. Top-down measurements are used to inform bottom-up estimates and highlight discrepancies, effectively improving knowledge on the location, magnitude, and sectors responsible for methane emissions. In recent years, significant advances in methane detection/quantification technologies have been made in the field of aerial and satellite remote sensing from satellites. Over a dozen methane sensing satellites are currently in orbit, either as single "stand-alone" instruments (e.g., TROPOMI) or constellations of multiple instruments that improves the ability to revisit regions of the world (e.g., GHGSat[6]). Broadly, methane sensing satellites are categorized as either point source imagers or global regional and area flux mappers [5]. Point source imaging satellites like GHGSat[6] and Carbon Mapper's/Planet's Tanager[7] detect and quantify methane point sources at fine spatial resolutions provided that the emission rate is above the detection threshold of the instrument. The fine spatial resolution of point source imagers allows for the identification of high-emitting point sources at ~25-30 meter pixel size , which in turn can be used to determine the facility linked to the emissions[8]. By contrast, global mapping and area flux satellites quantify methane emissions at regional or global scales at a coarser resolution and higher precision compared to point source imagers, with sectoral breakdowns of methane emissions available by leveraging spatially-explicit prior methane emission inventories like EDGAR and the gridded EPA-GHGI to inform the disaggregation[9–11].

MethaneSAT, which operated between March 2024 and June 2025, has a native ~100 × 400 m^2 sampling resolution, which enables the generation of methane emissions data at oil and gas basin scales (i.e., 220 × 440 km^2). in order to provide quantitative data for area emissions between the current suite of point source imagers and global flux mappers[5]. Examples of MethaneSAT XCH4 maps from which methane emissions data are generated can be found in Guanter et al.[12]. At a spatial resolution of 0.04° × 0.04° (≈4 × 4 km^2), Level 4 (L4) emissions data from MethaneSAT are among the finest resolution among the current swath of global regional and area flux mappers used to produce spatially-explicit emissions data products[5]. Other satellite systems continue to play a crucial role in advancing global methane science. Global-scale inversions using GOSAT and GOSAT-2 observations produce posterior estimates of methane emissions with resolutions varying from 4.0° × 5.0° (≈400 ×500 km^2)[13] to 1.0° × 1.0° (≈100 ×100 km^2)[14],

https://doi.org/10.5194/egusphere-2025-6126
Preprint. Discussion started: 30 December 2025

enabling long-term global trend detection and robust atmospheric constraints. TROPOMI has substantially improved spatial coverage and temporal density, supporting posterior emission products at 2.0° × 2.5° (≈200 × 250 km^2)[15] to 0.25° × 0.25° (≈25 × 30 km^2)[11], and continues to be an important dataset for global methane assessments. At regional scales, GOSAT and TROPOMI data have been demonstrated to produce finer-scaled posterior emissions estimates[9,10,16–18]. For instance, Veefkind et al.[18] derived 0.1° × 0.1° (≈10 ×10 km^2) emissions heatmaps in the Permian basin (US), demonstrating the strengths of these instruments when dense, high-quality (i.e., cloud-free) observations are available, especially from high-emitting regions such as the Permian basin which is one of the largest emitting oil/gas basins in the US (refer to Zhan et al. 2020). Area flux mappers continue to provide critical data on global-[14,19], country/continent-[9–11,17,20], and even regional-scale emissions patterns[16,18]. Producing emissions estimates at even finer administrative scales (state/province, county/district or individual oil/gas fields) is more challenging with lower-resolution and moderate precision instruments, as they typically require many cloud-free observations accumulated over months to years to resolve basin and sub-basin patterns, depending on the emissions magnitude and regional observing/meteorological conditions (cite Shen et al. 2022, ACP). Higher-resolution mapping with high precision measurements expand the ability to characterize emissions across these important administrative boundaries[1,3,10,21,22] supporting more targeted emission tracking and greater mitigation opportunity. MethaneSAT was designed to support these goals by delivering high-resolution mapping (≈4 × 4 km^2) over substantially wider swaths (220–440 km), combined high-precision measurements (cite Chris Miller AMT paper here), in turn providing an emissions tracking tool with a focus on oil and gas regions and their individual jurisdiction.

In this paper, we compile a set of methane emission data products derived using MethaneSAT observations from six distinct regions of the world encompassing the Permian oil and gas basin, the Eagle Ford oil and gas basin, the southeastern portion of the San Joaquin Valley, Turkmenistan and Uzbekistan sections of the Amu Darya oil and gas basin, and the Zagros Foldbelt in Iran and Iraq[12]. The regions were selected to represent a range of oil and gas production magnitudes, production characteristics (i.e., predominantly oil, gas, or a mixture of production), geography, and presence of non-oil and gas methane sources. We show sectoral allocated methane emissions for these regions and compare them to independent observations from other satellite-derived datasets and bottom-up inventories like the EPA gridded-GHGI and EDGAR. We also analyze oil and gas production normalized-intensities for oil and gas methane emissions and additionally apply this analysis across administrative boundaries. Finally, we perform a detailed county/district level analysis of MethaneSAT derived emissions and compare those estimates to bottom-up inventories to highlight specific areas showing large top-down/bottom-up discrepancies.

2 Observed regions and methane emissions analysis

2.1 Region descriptions

In this study, we present MethaneSAT observations from six distinct regions intersecting six countries, seven major oil and gas producing basins, and 207 districts/counties (i.e., Level 2 data from the Global Administrative Areas

https://doi.org/10.5194/egusphere-2025-6126
Preprint. Discussion started: 30 December 2025

database – GADM). All regions are named according to the primary oil and gas basin encompassed by MethaneSAT observations (Table S1), even if the full basin is not contained within the full observation domain.

Regions A, B, and C, are all located in North America, mostly in the USA. Region A (i.e., "Permian" observation domain) covers 99% of total oil and gas production within the Permian oil and gas basin[23] by combining a total of nine MethaneSAT observations with repeat coverage over the Midland and Delaware sub-basins, both associated with most of the oil and production in the larger Permian basin. The Permian basin, which is one of the highest producing basins in the world, is an oil-dominant basin (i.e., >50% of combined energy production is from oil) (Fig. S9) and a long legacy of resource development and a sustained production surge beginning in the 2010's, leading to significantgrowth in associated infrastructure development[24]. Region B (i.e., the "San Joaquin" observation domain) combines six observations over two distinct regions of the San Joaquin Valley - the Kings and Tulare counties which have been previously identified as regions with elevated methane emissions associated with livestock-related agricultural activity[25–27], and the Kern county associated with a mixture of oil and gas activity, landfills, and agricultural activity[25]. The San Joaquin oil and gas basin is a highly mature oil-dominant basin (Fig. S9) with production dating back to the late 1800's, with many older wells presently active. Oil and gas production within the San Joaquin basin has been steadily declining over the past four decades[28,29]. Region C (i.e., the "Eagle Ford" observation domain) utilizes three observations that principally target the Eagle Ford oil and gas basin in the US, but also extends into Mexico with some coverage of the Sabinas Basin where coal production first began in the country[30]. The Eagle Ford oil and gas basin is one of the youngest hydrocarbon basins we analyze in this work, with the first wells drilled in the late 2000's and an overall balance of oil versus gas production[31], with slightly higher gas production in the region we analyze[32] (Fig. S9).

Regions D, E, and F are all located in Asia and the Middle East. The Region D (i.e., " Amu Darya – UZB") combines six MethaneSAT observations covering most of the province of Qarshi (Uzbekistan) with some overlap into Turkmenistan. The Amu Darya – UZB region covers roughly 10% of the entire Amu Darya oil and gas basin and encompasses multiple oil and gas fields along the border of Uzbekistan and Turkmenistan[33]. In Region E (i.e., "Amu Darya – TKM"), we aggregate four observations that also cover a portion of the Amu Darya basin containing several major gas fields[33] and the city of Mary, the fourth largest city in Turkmenistan. Cumulatively, MethaneSAT observations in the Amu Darya basins from Turkmenistan and Uzbekistan encompass ~80% of total oil and gas production from the Amu Darya oil and gas basin based on production data[32]. The Amu Darya basin is dominated by gas production (i.e., >90% of combined production is gas) (Fig. S9), with the first productive gas fields discovered around the 1950's before development continued throughout the 1960's to 1980's[34]. For Region F (i.e., "Zagros Foldbelt") we combine six observations mostly covering the Zagros Foldbelt oil and gas basin in Iran with partial coverage over the Widyan oil and gas basin in Iraq (Fig. S2). The Zagros Foldbelt basin is a large oil-dominant basin (Fig. S9) with a long history of oil and gas production dating back to the early/mid 1900's with periodical investments stimulating modernization in the basin, producing a mixture of legacy and upgraded infrastructure[35].

2.2 Aggregation of emissions maps and independent comparisons

https://doi.org/10.5194/egusphere-2025-6126
Preprint. Discussion started: 30 December 2025

The methodology for inversion-based MethaneSAT emission data products and related uncertainty analysis are described in Appendix A and Appendix B sections of this paper. Each individual MethaneSAT emissions data product (or an emissions heatmap) is from a different day of observation and can be of variable dimensions depending on the viewing geometry with nadir viewing observations leading to ~220 km wide observations while off-nadir observations leading to upto ~440 km wide observation. The MethaneSAT platform had an agile observing mechanism with off-nadir viewing at upto 40 degrees on one side of it's observing track. We consider these variable observation domains over the same region of interest in our aggregation procedure of including multiple overpasses in order to produce a larger aggregated emission heatmap. To ensure consistency when aggregating repeat observations, we reproject all MethaneSAT gridded emissions estimates onto a common global 0.04° × 0.04° grid (Fig. S1) using an equal-area weighting approach that preserves total methane mass. Then, we average the methane emission rates over each grid cell for each overlapping emission heatmap and combine to produce an aggregated methane emission heatmap. We also apply the same approach using the median during aggregation as an additional test of sensitivity and find broad consistency between the two methods (Fig. S10).

We perform intercomparisons of total methane emissions estimates from MethaneSAT to other spatially explicit methane emissions data from both bottom-up and top-down methodologies. In all intercomparisons, we match the spatial domains to ensure that the same regions are being compared. In addition to total methane emissions, we also produce comparisons of available literature-based emissions from different sectors (i.e., oil and gas and non-oil and gas emissions). From the bottom-up inventories, we specifically compare MethaneSAT to the EPA gridded greenhouse gas inventory (ie., gridded EPA-GHGI)[3] for observations in the US, and to EDGAR[4] (version EDGAR_2025_GHG) and CAMS v6.2[36] for regions outside of the US. The EPA-GHGI provides annual estimates for 2020, while EDGAR and CAMS v6.2 both report annual emissions for 2024. The EPA-GHGI inventory[3] and the EDGAR[4] global bottom-up inventory provides emissions estimates for member countries under the UNFCCC. Other bottom-up inventories that are used as prior information for satellite-based inversions include the GFEI v2[37] and CAMS v6.2[36]. Our comparisons to top-down satellite-based observations vary by region and are presented later in the Results section.

2.3 Sectoral disaggregation and methane intensity calculations

We attribute MethaneSAT methane emissions to broad methane sectors by leveraging a combination of bottom-up inventories and Carbon Mapper detected point sources in a composite prior inventory using a simple proportional allocation, where e_i are MethaneSAT emissions from sector i, E are total methane emissions estimates from MethaneSAT, $p_{i,j}$ are emissions estimates from prior inventory j and sector i, and P_j are total methane emissions from prior inventory j.

$$e_i = E \frac{\sum_j p_{i,j}}{\sum_j P_j}$$

https://doi.org/10.5194/egusphere-2025-6126
Preprint. Discussion started: 30 December 2025

To reduce structural omissions in any single inventory, we construct a composite dataset as the sum of multiple independent inventories (Fig. S5). This composite data approach has precedents in methane inversion frameworks [19,20,38] where multisource priors or spatially-explicit inventories are used to improve completeness and robustness. For bottom-up inventories – we incorporate the gridded EPA-GHGI[3], EDGAR[4], EIME[39], CAMS v6.2[36], and GFEI v2[37] as inputs, which are all mapped at their native spatial resolution of 0.1° x 0.1°. For any region, we combine emissions estimates from two bottom-up inventories with Carbon Mapper distinct point sources to produce the composite dataset. For regions within the US, we use the EPA-GHGI and EDGAR as inputs for non-oil and gas sources, and the EI-ME and EDGAR for oil and gas sources. For regions outside of the US, we use CAMS v6.2 and EDGAR as inputs for non-oil and gas sources, and the GFEI v2 and EDGAR as inputs for oil and gas sources. Other combinations of these bottom-up inventories, and their impacts on the resulting sectoral breakdown of emissions, are provided in the SI (Fig. S7; Fig. S8). We include persistence-adjusted distinct point source measurements from Carbon Mapper[40] provided they are sources that have been observed at least three times. To translate the composite dataset to our aggregate MethaneSAT emissions heatmaps, we apply an equal area weighting-approach of the composite dataset to the same 0.04° x 0.04° global grid. To better account for regions where granular oil and gas infrastructure data is limited (i.e., regions outside of the US), we spatially aggregate oil and gas methane emissions estimates from the composite prior by a factor of four (i.e., from the native 0.1° x 0.1° resolution to 0.4° x 0.4°) while conserving the mass of emissions. A sensitivity test of this approach finds that oil and gas emission estimates increase with decreasing spatial resolution for regions outside of the US with relatively little change in oil and gas emissions estimates for regions in the US (Fig. S6). We allocate total methane emissions estimates from MethaneSAT to broad sectors outlined as oil and gas (i.e., upstream and midstream sectors), waste (i.e., solid waste disposal landfills), agriculture (i.e., manure management, enteric fermentation, and agricultural soils such as rice cultivation), coal, and other non-oil and gas sources (i.e., post-meter emissions, wastewater treatment, chemical processing, etc). For grid cells where we estimate over 100-times the total methane emissions contained within a single grid compared to the composite inventory, we assign emissions as having an "unknown" origin and incorporate their relative percentage contributions into the uncertainty calculations related to sectoral disaggregation. Methane emissions from wetlands and termites are not included in the sectoral disaggregation since their combined methane emissions are less than 1% of total methane emissions from the observed regions based on data from WetCHARTs (v1.3.1) [41] and Jung et al[42].

We assess oil and gas methane intensity using two distinct and complementary metrics:

1. Marketed gas production-normalized methane intensity, defined as the ratio of oil and gas methane emissions to marketed methane production (i.e., loss rates).

2. Energy-normalized methane intensity, defined as the ratio of oil and gas methane emissions to total energy production measured as marketed oil and gas production in gigajoules (GJ) (i.e., energy-normalized intensity).

We estimate loss rates from reported marketed natural gas production volumes, adjusted for the methane content of the produced gas, which is consistent with the oil and gas decarbonization charter's metric to track methane intensity reduction goals[43]. Oil and gas production data are sourced from Wood Mackenzie for the year 2024[32]. The energy-

https://doi.org/10.5194/egusphere-2025-6126
Preprint. Discussion started: 30 December 2025

normalized methane intensity metric reflects the climate impact relative to saleable energy products and aligns with methodologies used by the International Energy Agency (IEA) for comparing methane intensities across regions (www.iea.org). In contrast, the gas production-normalized methane intensity (i.e., loss rate) provides a measure of a region's gas conservation performance - indicating the proportion of produced gas lost through leakage, venting, flaring, or other losses. This metric, normalized by marketed gas production, is consistent with the methane intensity frameworks established under the Oil and Gas Methane Partnership (OGMP) 2.0, supporting direct comparison between industry-reported methane targets and measurement-based assessments. We assume a methane gas composition in natural gas of 80% for all intensity metric calculations.

3 Results

We incorporate a total of 33 MethaneSAT observations from six separate regions of the world including the United States (USA), Mexico (MEX), Turkmenistan (TKM), Uzbekistan (UZB), Iran (IRN), and Iraq (IRQ) (Table S1). The observation dates of MethaneSAT data span one year from May 2024 to May 2025. Total methane emissions from the single scenes ranged from 353 (95% c.i.: 268 - 446) t/h in the Permian oil and gas basin in the United States (USA) at in October 2025, to 29 (95% c.i.: 16 – 46) t/h measured in the Eagle Ford oil and basin in December 2024 (Table S1). We aggregate these single emission heatmaps together to form regional estimates of methane emissions (see Methods - Section 2.2).

3.1 Methane emissions by region and sector

Total methane emissions for the regional six observations domains are: 454 t/h (95% c.i.: 351 – 563 t/h) in the Permian, 251 t/h (95% c.i.: 189 – 321 t/h) in the Zagros Foldbelt, 192 t/h (95% c.i.: 146 – 242 t/h) in Amu Darya – UZB, 188 t/h (95% c.i.: 141 – 239 t/h) in Amu Darya – TKM, 127 t/h (95% c.i.: 95 – 162 t/h) in the San Joaquin, and 114 t/h (95% c.i.: 83 – 149 t/h) in the Eagle Ford (Fig. 1).

We attribute methane emission estimates from MethaneSAT to specific methane sectors and find varied sectoral emissions among the different observation domains, reflecting a diversity of methane emitting sources among the different regions. The Permian contains the highest percentage of oil and gas methane emissions at 90% (95% c.i.: 64 – 100%), followed by the Zagros Foldbelt at 81% (95% c.i.: 58 – 100%), the Eagle Ford at 70% (95% c.i.: 41 – 99%), Amu Darya – UZB at 52% (95% c.i.: 37 – 70%), Amu Darya – TKM at 52% (95% c.i.: 38 – 66%), and the San Joaquin with the lowest percentage of oil and gas emissions at 24% (95% c.i.: 18 – 31%) (Fig. 2). Among non-oil and gas sources, the dominant sector among the observation domains was consistently agricultural emissions associated with livestock like concentrated animal feeding operations (ie., CAFO's) and manure management (Fig. 2). After the agricultural sector, non-oil and gas emissions from the waste and other (i.e., wastewater treatment, post-meter, stationary combustion, etc) sources were the most prominent emission sectors in Amu Darya – UZB, Amu Darya – TKM, Zagros Foldbelt, and San Joaquin (Table S2). For the Eagle Ford region, the waste and coal sectors

https://doi.org/10.5194/egusphere-2025-6126
Preprint. Discussion started: 30 December 2025

were the highest methane-emitting sectors from non-oil and gas sources after the agricultural sector. All sectoral emissions by region can be found in Table S2.

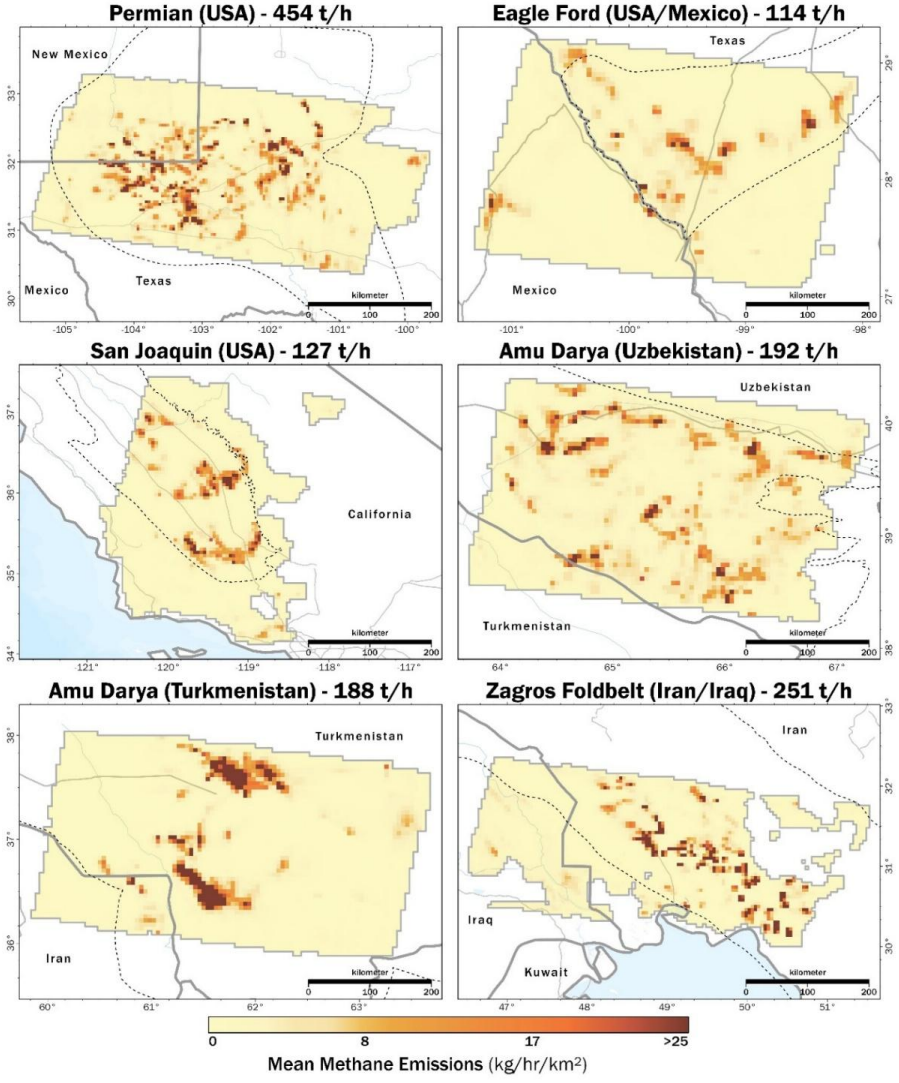

Fig. 1: Maps of aggregated MethaneSAT methane emissions from the Permian (US), Eagle Ford (US, Mexico), San Joaquin (US), two separate Amu Darya regions in Turkmenistan and Uzbekistan, and the Zagros Foldbelt (Iran, Iraq). Notable geographical boundaries are illustrated in the maps, including country boundaries in solid grey, and oil and gas basin boundaries in dashed outlines.

https://doi.org/10.5194/egusphere-2025-6126
Preprint. Discussion started: 30 December 2025

We calculated methane intensities based on marketed gas and total energy (i.e., combined oil and gas) production for 2024[32] from all aggregated domains and for notable administrative/sub-basin boundaries among the observation domains (Fig. 3). Loss rates among the six regions measured in this work consistently exceeded the 0.2% goal set within the Oil and Gas Climate Initiative (OGCI)[44]. The Eagle Ford region had the lowest loss rates at 2.4% (95% c.i.: 1.4 – 3.4%), followed by the Permian at 2.6% (95% c.i.: 1.9 – 3.5%), Amu Darya – TKM region at 2.9% (95% c.i.: 2.1 – 3.7%), Amu Darya – UZB region at 3.7% (95% c.i.: 2.7 – 5.0%), the San Joaquin region at 12.1% (95% c.i.: 8.9 – 16.0%), and the highest gas-production normalized loss rates in the Zagros Foldbelt at 18.6% (95% c.i.: 13.4 – 23.8%). For energy-normalized methane intensities, which accounts for combined marketed oil and gas production and matches the metric used by the International Energy Agency (IEA) to track progress towards methane reduction targets[45], we estimate the lowest energy-normalized intensities for the Zagros Foldbelt at 0.16 (95% c.i.: 0.12 – 0.20) kg CH_4/GJ and the Permian at 0.16 (95% c.i.: 0.12 – 0.21) kg CH_4/GJ, followed by the Eagle Ford at 0.21 (95% c.i.: 0.12 – 0.30) kg CH_4/GJ, the Amu Darya – TKM region at 0.40 (95% c.i.: 0.29 – 0.51) kg CH_4/GJ, the San Joaquin region at 0.42 (95% c.i.: 0.31 – 0.55) kg CH_4/GJ, and the highest energy-production normalized methane intensities in the Amu Darya – UZB region at 0.51 (95% c.i.: 0.27 – 0.69) kg CH_4/GJ. We observed similar intensity metrics, both for marketed gas-production and oil and gas-production normalized intensities, within specific oil and gas basin boundaries compared to the broader observation domains (Fig. 2; Table S3).

We compare methane emissions estimates and methane intensities across sub-basins and administrative boundaries (e.g., countries/states) (Fig. 2). Within the Midland and Delaware subbasins of the Permian (Fig. 2), we estimate oil and gas methane emissions of 178 (95% c.i.: 132 – 224) t/h and 112 (95% c.i.: 81 – 143) t/h respectively, with comparable marketed gas-production normalized loss rates of 2.0%. The Permian basin transects both the New Mexico and Texas state boundaries, where we estimate oil and gas methane emissions of 67 (95% c.i.: 43 – 90) t/h and 338 (95% c.i.: 249 – 427) t/h respectively from MethaneSAT observations. We find over twice the marketed gas- and energy-production normalized methane intensity values in Texas at 3.1% and 0.19 kg CH_4/GJ compared to New Mexico at 1.3% and 0.08 kg CH_4/GJ (Fig. 2; Table S3). The same state-level comparison restricted to the Delaware subbasin boundary shows a similar discrepancy in the magnitude of the methane intensities with the Texas portion of the Delaware subbasin having a marketed gas-production normalized intensity of 2.8% compared the New Mexico portion of the Delaware subbasin at 1.0%. Similar trends have also been observed in recent TROPOMI-based estimates by Varon et al. (2025), with New Mexico showing decreasing methane intensities from 4.5% in 2019 to 2.1% in 2023 plausibly associated with state-wide policies requiring operators to reduce methane intensities below 2% by 2026[46].

In the Eagle Ford, we note that nearly all oil and gas emissions occur within the US compared to Mexico, with methane emissions in Mexico largely originating from agricultural sources and coal (Fig. 2; Table S6). Nearly all oil and gas infrastructure is located within the Eagle Ford oil and gas basin boundary, with sparse infrastructure in Mexico compared to the US[47]. MethaneSAT observations in Mexico largely transect the Burgos basin, a major natural gas-producing basin. Although geologically similar to the Eagle Ford basin, daily gas production in the Eagle

https://doi.org/10.5194/egusphere-2025-6126
Preprint. Discussion started: 30 December 2025

290 Ford exceeds 7,000 MMcf/day compared to 30 MMcf/day from the Burgos, highlighting stark differences in the
291 degree of development between the basins which we can clearly observe in the oil and gas methane emission
292 estimates from MethaneSAT.

293 In the Zagros Foldbelt region, we find that the methane intensities in the Zagros Foldbelt oil and gas basin in Iran
294 (i.e., 25.5% and 0.24 kg CH_4/GJ) from are over five-times higher than the bordering Widyan oil and gas basin in
295 Iraq (i.e., 4.2% and 0.03 kg CH_4/GJ), noting that MethaneSAT observations only cover 17% of combined oil and gas
296 production in the Widyan basin compared to 59% from the Zagros Foldbelt basin (Fig. S9). Within the Amu Darya
297 basin boundary, we find higher methane intensities from the Amu Darya – TKM region at 4.1% and 0.57 kg CH_4/GJ
298 compared to the Amu Darya – UZB at 3.6% and 0.49 kg CH_4/GJ (Table S3). Collectively, MethaneSAT observations
299 from Amu Darya – TKM and Amu Darya – UZB cover 79% of total oil and gas production within the Amu Darya
300 oil and gas basin[32] (Fig. S9) with an associated gas-production normalized intensity of 3.8% and an energy-
301 normalized intensity of 0.53 kg CH_4/GJ.

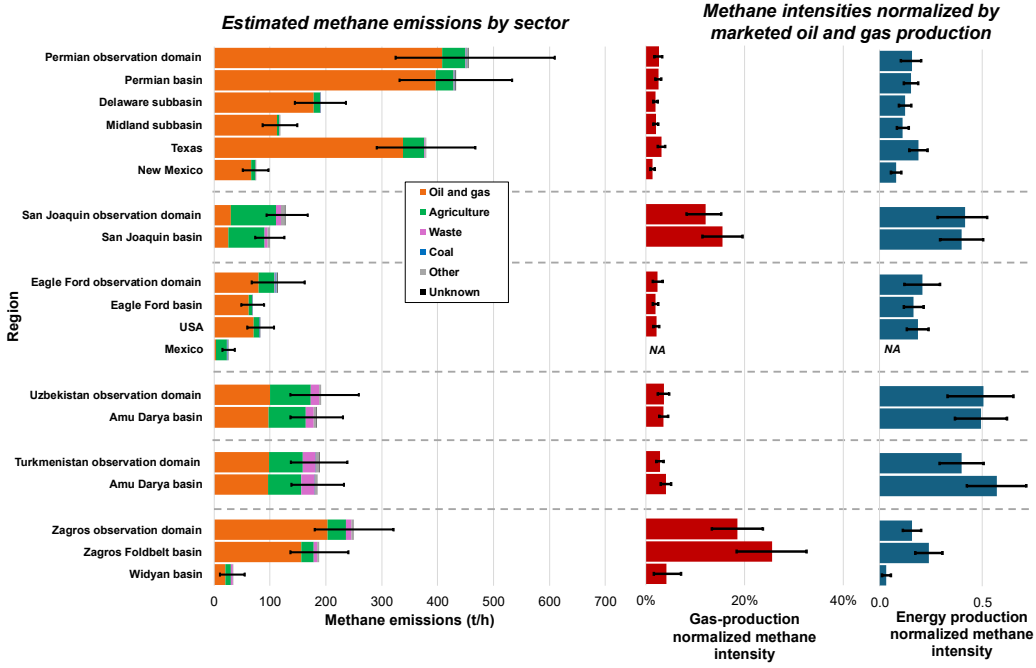

302

303 **Fig. 2:** Sectoral breakdown of methane emissions from aggregated MethaneSAT emissions for full observation
304 domains, and subregions defined by administrative boundaries and oil and gas basin and sub-basins. Methane
305 intensities including marketed gas-production normalized intensities and energy-normalized production intensities
306 are calculated for all observation domains and subregions[32].

307

308

309

https://doi.org/10.5194/egusphere-2025-6126
Preprint. Discussion started: 30 December 2025

3.2 Comparison of MethaneSAT-derived emissions to independent estimates

Our estimates of methane emissions and sectoral breakdowns from MethaneSAT match closely with other independent estimates for the same spatial domains from other satellite observations (Fig. 3). In the Permian basin, a region that has been extensively surveyed using a wide range of methods from ground-based surveys [48,49], tower-based observations [50,51], aerial-based surveys [52–55], and satellite-based observations [9–11,14,56–58], we find our estimate of oil and gas emissions of 408 (95% c.i.: 303 - 516) t/h for 2024 are similar to the most recent estimates from TROPOMI inversions by Varon et al.[58], and generally higher than older satellite-based estimates from 2020 and 2019 (Fig. 3). Our estimated marketed gas-production normalized methane intensity within the Permian basin domain of 2.5% (95% c.i.: 1.9 – 3.1%) for the Permian closely aligns with recent estimates from MethaneAIR for 2023 at 2.4% (95% c.i.: 1.5 – 3.2%)[59] (Table S3), noting that methane intensities from MethaneAIR are calculated using gross gas production instead of marketed gas production. Our estimate of non-oil and gas emissions in the Permian region of 41 (95% c.i.: 26 - 75) t/h closely matches the most recent comparable dataset from Varon et al. (2025) of 48 t/h, but higher than older estimates from GOSAT[14,20].

In the Eagle Ford region, we find that our total emissions estimate of 114 (95% c.i.: 83.6 - 150) t/h is higher than most other independent satellite-based observations (Fig. 3) with differences largely attributable to higher oil and gas emission estimates from MethaneSAT. Our estimated marketed gas production-normalized loss rate within the Eagle Ford of 1.9% (95% c.i.: 1.3 – 2.8%) closely matches recent MethaneAIR measurements from 2023 of 2.0% (95% c.i.: 1.6 – 2.7%)[59], implying that the elevated emission observations from MethaneSAT may reflect increasing natural gas production in recent years, especially from the Austin Chalk Play where natural gas production has nearly quadrupled since 2014[31].

In the San Joaquin region, we estimate 30 (95% c.i.: 20 – 41) t/h from oil and gas sources which compares well with multiple independent satellite-based estimates (Fig. 3). We find elevated marketed gas-production normalized loss rates within the San Joaquin oil and gas basin boundary at 15.5% (95% c.i.: 11.4 – 19.6%), which is also observed in Omara et al.[39] with a gas production-normalized methane intensity of 15.3% for the entire San Joaquin oil and gas basin in 2021. The San Joaquin basin is characterized by a large proportion of marginally-producing well sites [60], which are typically associated with increased methane loss rates[61]. We find higher emissions from non-oil and gas sources (i.e., 97 t/h) within the San Joaquin region compared to older satellite-based estimates[14,20,62] (Fig. 3), which may reflect changes in the dairy industry for the region. While oil and gas production has declined in recent decades, milk production has grown 153% in the state of California since the early 1980's, with most of the growth occurring within Tulare county[63].

In the Amu Darya – UZB region, our estimates of oil and gas emissions at 100 (95% c.i.: 57 – 137) t/h support the higher range of 39 to 110 t/h (Fig. 3) found in independent satellite-based estimates. Oil and gas production within Uzbekistan has stabilized/declined in past decades[64], supporting similar oil and gas methane emission estimates from past satellite-based inversions to estimates from MethaneSAT (Fig. 3). Our estimates of non-oil and gas emissions from the Amu Darya region of 92 (95% c.i.: 55 – 134) t/h exceed those from independent estimates which range from 14 to 45 t/h (Fig. 3). Our total methane emission estimates from the Amu Darya region are also higher than

https://doi.org/10.5194/egusphere-2025-6126
Preprint. Discussion started: 30 December 2025

other independent estimates, albeit with statistical overlap for estimates from GOSAT estimates in North Africa [65] and TROPOMI estimates in the Middle East and North Africa[66]. Trends in methane emissions in Uzbekistan, as reported to the UNFCCC from 1990-2012 [67], indicate increasing emissions from non-oil and gas sources like enteric fermentation, landfills, and wastewater treatment versus declining/stable emissions from the energy sector. Estimates from MethaneSAT for the Amu Darya – UZB region may indicate a continuation of these trends.

In the Amu Darya – TKM region, we find consistently higher estimates of methane emissions from MethaneSAT compared to other satellite-based observations. Only one other satellite-based observation contains full sectoral emissions for the region from GOSAT observations[14], which finds negligible non-oil and gas emissions (Fig. 3). Non-oil and gas emissions from the Amu Darya – TKM region are predominantly from agricultural and waste sectors respectively at 60 (95% c.i.: 38 – 85) t/h and 24 (95% c.i.: 15 – 32) t/h located in the North of the observation domain over the city of Mary (Fig. 1). Our estimates of marketed gas-production normalized methane intensity metrics in the Amu Darya – TKM region of 2.6% (95% c.i.: 1.7 – 3.6%) is lower than the 4.9% estimated from satellite-based observations for 2019[17], although the MethaneSAT observations exclude the South Caspian area, a region that has been repeatedly observed with large point source emissions associated with oil and gas infrastructure[68–70].

Our total methane emission estimates from the Zagros Foldbelt region overlap with multiple satellite-based observations (Fig. 3), although we estimate higher emissions attributable to non-oil and gas sources compared to Worden et al.[14] which is the only satellite-based observation that provides comprehensive sectoral disaggregation of methane emissions for the region. Our estimates of oil and gas emissions are lower than both Shen et al.[19] and Worden et al.[14], which could indicate declining oil and gas emissions in the region. However, this contradicts production trends in both Iran and Iraq which both show increasing gas production over the past decade based on the International Energy Agency[71,72]. We find high marketed gas production normalized loss rates in the Zagros Foldbelt oil and gas basin at 25.5% (95% c.i.: 18.5 – 32.6%), which is over ten-times higher than country level estimates of 0.8% for Iran from satellite-based observations from 2019[17]. A comparison of methane emissions estimates within the MethaneSAT observation domain from the same study[17] are less than half the emissions estimated by MethaneSAT, which could contribute to the observed differences in methane intensities, in addition to other factors (i.e., variations in the spatial representation of the loss rate estimates, production characteristics, sectoral disaggregation methods, and study year).

https://doi.org/10.5194/egusphere-2025-6126
Preprint. Discussion started: 30 December 2025

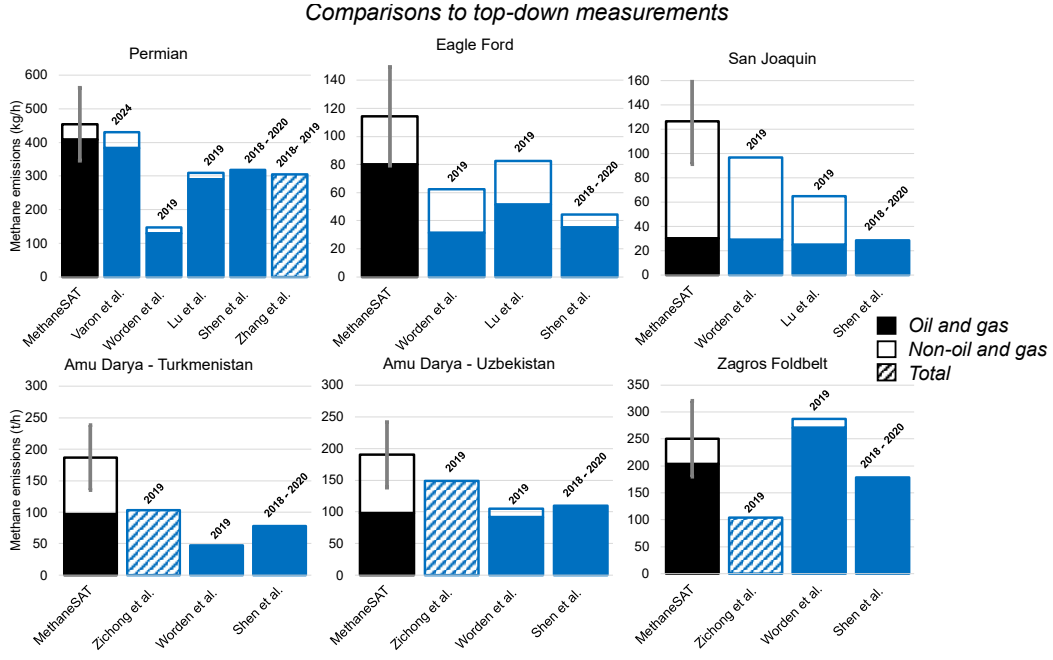

Fig. 3: Comparisons of oil and gas and non-oil and gas methane emission estimates from MethaneSAT to recent (ie., post-2018) independent top-down observations from peer-reviewed studies. Measurements years are indicated above the bars. The number of available top-down studies available for comparison vary by region, with the highest number of independent estimates available for the Permian region. Note that emission estimates from Shen et al. (2023) are only associated with the oil and gas and coal sectors. Independent studies that do not disaggregate methane emissions by sector are indicated by dashed bars.

In the US, we find that MethaneSAT observations from 2024-2025 are consistently higher than 2020 estimates from the gridded EPA-GHGI by a factor of 2-5. This finding echoes recent results from comprehensive aerial sampling campaign from MethaneAIR[59], and a broader trend of top-down observations exceeding estimates from bottom-up inventories[1]. We find that both oil and gas, and non-oil and gas emissions estimates from MethaneSAT exceed those from the gridded EPA-GHGI, highlighting broad discrepancies among multiple methane-emitting sectors. Oil and gas emissions estimates from MethaneSAT are four-times higher compared to the gridded EPA-GHGI in the Permian and Eagle Ford regions and two-times higher in the San Joaquin. Emissions from the waste sector are consistent between MethaneSAT and the gridded EPA-GHGI, with most differences from non-oil and gas sources occurring from the agricultural sector with MethaneSAT finding higher estimates by a factor of four in the Eagle Ford and Permian, and a factor of two in the San Joaquin. For all three regions in the US, oil and gas emissions were consistently higher than the EPA-GHGI by a greater degree when compared to non-oil and gas emissions.

For regions outside of the US, we compare MethaneSAT observations to bottom-up emission inventories from EDGAR[4] and CAMS v6.2[36]. For the Zagros Foldbelt, we find closer agreement to CAMS v6.2 compared to EDGAR. In Amu Darya – UZB, we find comparable estimates of oil and gas emissions from EDGAR and CAMS

https://doi.org/10.5194/egusphere-2025-6126
Preprint. Discussion started: 30 December 2025

v6.2, but our estimates of non-oil and gas emissions are twice as high as the bottom-up estimates, largely due to increased emissions related to agriculture. We see the largest discrepancies between MethaneSAT and bottom-up inventories in the Amu Darya – TKM region, with MethaneSAT estimates of methane emissions more than five-times higher than the 33 t/h and 22 t/h estimated within CAMS v6.2 and EDGAR respectively (Fig. 4). Persistence-adjusted point source detections from Carbon Mapper alone amount to 20 t/h in the Amu Darya – TKM region (Fig. S4), implying that bottom-up estimates are likely underestimating emissions in the region.

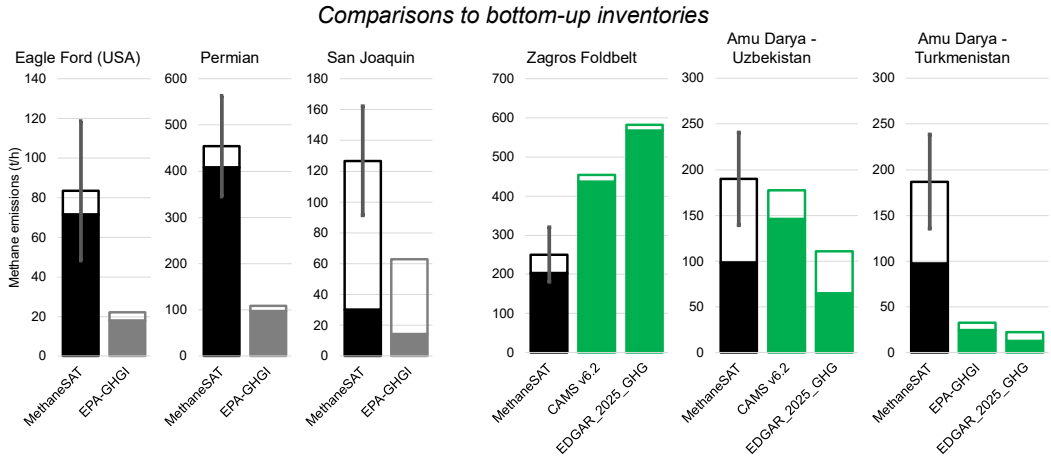

Fig. 4: Comparisons of oil and gas and non-oil and gas methane emission estimates from MethaneSAT to bottom-up inventories. In the US, we compare MethaneSAT emission estimates to the EPA-GHGI which is a national greenhouse gas inventory used to report methane emissions and inform policy. For regions outside of the US, we compare MethaneSAT emissions to CAMS v6.2 and EDGAR_2025_GHG, both global bottom-up methane emissions datasets that are commonly used to inform prior emissions estimates in top-down inversions. Note that for the Eagle Ford region, we restrict our comparison to the EPA-GHGI only for the region contained in the US, hence the lower total emissions estimates compared to the full observation domain.

3.3 Insights from MethaneSAT emissions estimates across jurisdictions

We quantify methane emissions from MethaneSAT for jurisdictions (i.e., second-level administrative divisions - county/districts) from all six regions analyzed in this work. We investigate differences between bottom-up inventory estimates within jurisdictional bounds using the high-resolution data provided from MethaneSAT observations.

In the Permian region, the five highest emitting counties (i.e., Reeves, Eddy, Culberson, Lea, and Pecos) collectively contribute 41% of total methane emissions from the region (Fig. 5). We find that total methane emissions estimates are consistently higher than the gridded EPA-GHGI across multiple counties/districts, with the difference driven by oil and gas emissions (Fig. 5). Methane emissions quantified by MethaneSAT within the Permian basin are predominantly from oil and gas sources, a finding repeated in multiple independent observations [10,11,20,55,56,58]. In Reeves County (Texas), where we observe the highest total methane emissions in the region, estimates are roughly

https://doi.org/10.5194/egusphere-2025-6126
Preprint. Discussion started: 30 December 2025

10-times higher than the gridded EPA-GHGI national inventory. In Eddy and Lea counties, both located in the state of New Mexico, the bottom-up inventory differences are less pronounced at a factor of two. These trends also reflect our findings of methane intensities between the states of Texas and New Mexico (Fig. 2), where intensities relative to gas and oil and gas production in Texas over twice those in New Mexico. Discrepancies between the EPA-GHGI and MethaneSAT in non-oil and gas emissions are less pronounced in the Permian, which also reflects the dominance of oil and gas emissions.

In the Eagle Ford region, the five highest emitting counties (ie., Webb, Dimmit, Lasalle, Maverick, and McMullen) cumulatively account for 63% of total methane emissions within the Eagle Ford region (Fig. 5). MethaneSAT data shows consistently higher emissions compared to the EPA-GHGI in the US, and to EDGAR in Mexico (Fig. 5). The three highest emitting counties, Webb, Dimmit, and LaSalle, all have emissions estimates that are 3-4 times higher than the EPA-GHGI. By contrast, MethaneSAT emissions estimates in Maverick County are nearly 20-times higher than the EPA-GHGI, driven by differences in both oil and gas and non-oil and gas methane emissions. All three of the counties located within Mexico contain negligible emissions estimates from EDGAR. The highest emitting county we analyzed within Mexico is Sabinas County located within the Sabinas basin, Mexico's largest coal-producing region [73]. Several distinct point sources detected by Carbon Mapper and IMEO-MARS (i.e., satellite: EMIT – NASA) attributable to coal emissions are also contained within Sabinas County (Fig. S3), with point source emission rates detected by EMIT-NASA ranging from 1.4 to 4.4 t/h, and Carbon Mapper reporting a persistence-adjusted methane emission rate of 1.8 t/h (95% c.i.: 1.5 – 2.1 t/h), similar to total methane emissions attributable to coal sources from MethaneSAT for this region of 1.6 t/h (95% c.i.: 1.1 – 2.2 t/h).

In the San Joaquin region, the five highest emitting counties measured by MethaneSAT (ie., Tulare, Kings, Kern, Fresno, and Madera) account for 84% of total methane emissions within the San Joaquin region. All three counties show increased emissions relative to the EPA-GHGI by a factor of 2-3. The MethaneSAT observation domain in the San Joaquin Valley encompasses a mixture of oil and gas and non-oil and gas methane emissions sources, with predominantly non-oil and gas methane emissions focused in Kings and Tulare counties, and mixture of oil and gas, agriculture, and waste emissions in Kern County (Fig. 5). The degree of difference between the EPA-GHGI and MethaneSAT estimates in San Joaquin region is lower than the Eagle Ford or Permian, potentially due to the relative lack of oil and gas methane emissions which has been highlighted as a major sector responsible for discrepancies between top-down and bottom-up estimates in the US[21]. The diversity in the sectoral contributions of methane emissions in the San Joaquin region is also seen in the mapping of distinct point sources from IMEO-MARS and Carbon Mapper (Fig. S3), showing two clear regions of dense point source detections related to concentrated animal feeding operations (CAFO's) in Kings and Tulare counties and point sources related to oil and gas emissions in Kern County (Fig. 5). Multiple studies have highlighted the prominence of emissions from dairy sources in Kings and Tulare counties [25,26,62,74]. Despite rising milk production in the Tulare county region, the number of dairy operations dropped since the 1990's, reflecting structural changes to the dairy industry in California like the enlargement of herd sizes and consolidation of smaller farms into larger operations [63]. Most oil and gas emissions estimated by MethaneSAT follow a semi-circular pattern enveloping the southeastern edge of the San Joaquin oil and gas basin, a

https://doi.org/10.5194/egusphere-2025-6126
Preprint. Discussion started: 30 December 2025

pattern also observed in other spatially-explicit methane emission estimates like the EI-ME [39] and GFEI v2 [37]. This portion of the San Joaquin oil and gas basin corresponds to a relatively dense area of oil and gas infrastructure including refineries and processing plants.

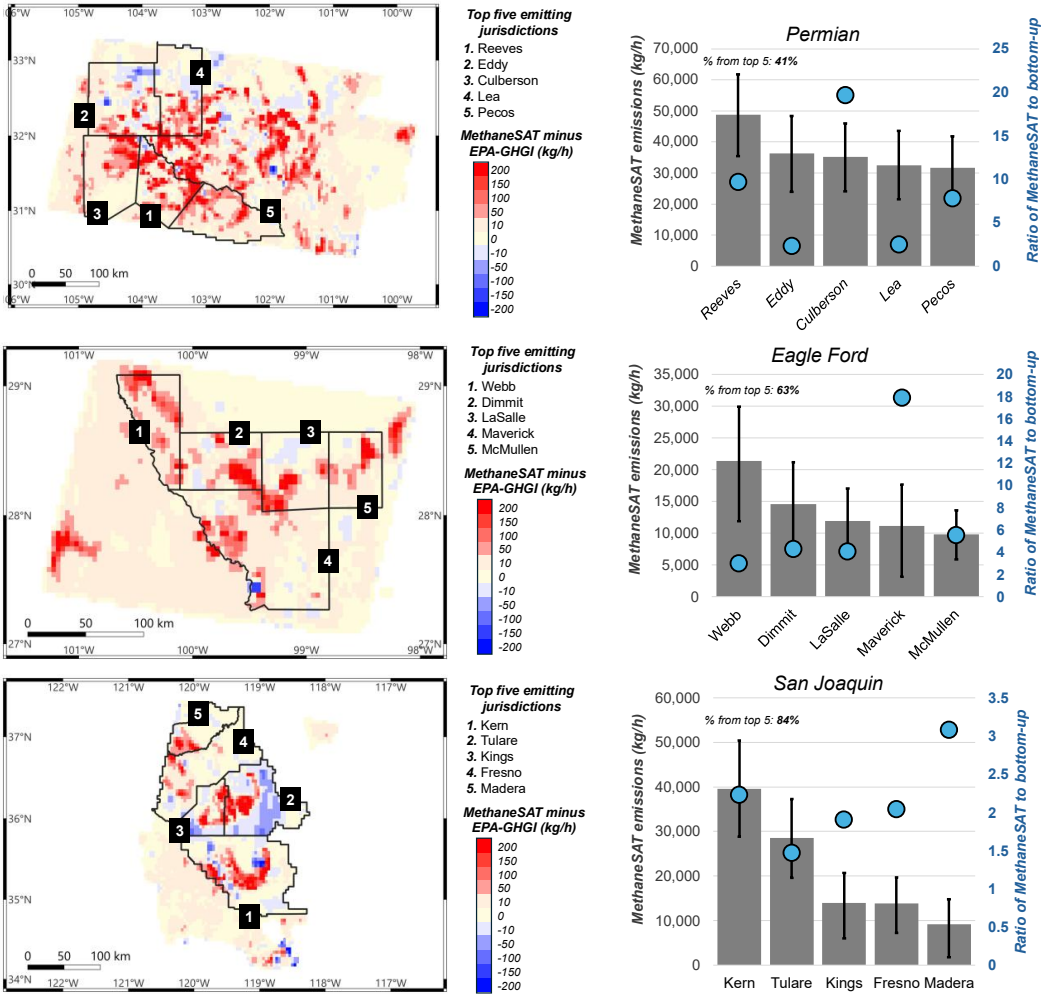

Fig. 5: Left column displays maps of the differences between MethaneSAT emissions estimates and the gridded EPA-GHGI at the county/district level. Right column displays the county/districts with the five highest MethaneSAT emissions estimates and the respective ratios compared to bottom-up inventories (i.e., MethaneSAT divided by EPA-GHGI). The percentage of total emissions accounted for by the top five emitting counties/districts are indicated above each respective barplot.

https://doi.org/10.5194/egusphere-2025-6126
Preprint. Discussion started: 30 December 2025

Methane emissions are evenly distributed among jurisdictions within the Amu Darya – UZB region, with the five highest emitting counties (ie., G'uzor, Nurobod, Usmon Yusupov, Muborak, and Buzoro) collectively emitting 34% of emissions for the entire region (Fig. 5). Comparisons of total methane emissions estimates from MethaneSAT to bottom-up estimates from EDGAR show variable discrepancies in emissions estimates (Fig. 5). Broadly, we find that MethaneSAT estimates higher methane emissions in the North in Nurobod and Buxoro, but finds similar emissions to EDGAR in the South in G'uzor and Usmon Yusupov. The southern portion of the MethaneSAT observation domain contains most of the known oil and gas infrastructure in the region[47], including multiple distinct point source detections from IMEO-MARS and Carbon Mapper (Fig. S4). Increased methane emissions in the North are the primary explanation for why our overall estimates of methane emissions in the Amu Darya – UZB region are higher than multiple independent observations from both satellite and bottom-up inventories (Fig. 2; Fig. 3).

Over half (ie., 64%) of total methane emissions in the Amu Darya – TKM region originate from the five highest emitting districts of Murgad, Sarahs, Baramaly. Turkmengala, and Sakarcage (Fig. 6). We consistently find elevated emissions estimates from MethaneSAT compared to bottom-up estimates from EDGAR (Fig. 7) to a greater degree than any of the regions we analyzed in this work. In Sarahs District which borders the city of Mary, total emissions estimates from MethaneSAT at 32 t/h are nearly 60-times higher than emissions estimates from EDGAR, due to elevated oil and gas methane emissions estimated by MethaneSAT. Across four of the five highest emitting districts/cities in the Amu Darya – TKM region, emissions estimate from MethaneSAT are a factor of 10-60 times higher than EDGAR (Fig. 7), with the exception being Türkmengala District. We also note broad discrepancies observed in the northern portion of the Amu Darya – TKM region in between Bayramaly and Sakarcage and around the city of Mary (Fig. 7). In this region, we find a high density of methane hotspots detected by TROPOMI - Sentinel-5P[22], but a lack of point source detections from other instruments (ie., Carbon Mapper, EMIT, PRISMA) (Fig. S4) potentially caused by limited instrument targeting in this area or by higher emissions dispersed across wider areas that may be below the detection limit of high-emitting point source detection instruments.

Across districts in the Zagros Foldbelt region we find consistent agreement, and even underestimation, of methane emissions from MethaneSAT compared to EDGAR (Fig. 6). Cumulatively, the top five highest emitting districts (Ahvaz, Ramhormoz, Behbahan, Kohgiluyeh, and Gachsaran) are responsible for 66% of total methane emissions in the Zagros Foldbelt region. Except for Kohgiluyeh, MethaneSAT emissions estimates for all these jurisdictions are within a factor of 2 compared to EDGAR. Residual emissions in the region show neighboring positive and negative values, especially for oil and gas emissions following the NE-SW domain of the Zagros Foldbelt basin (Fig. 7).

https://doi.org/10.5194/egusphere-2025-6126
Preprint. Discussion started: 30 December 2025

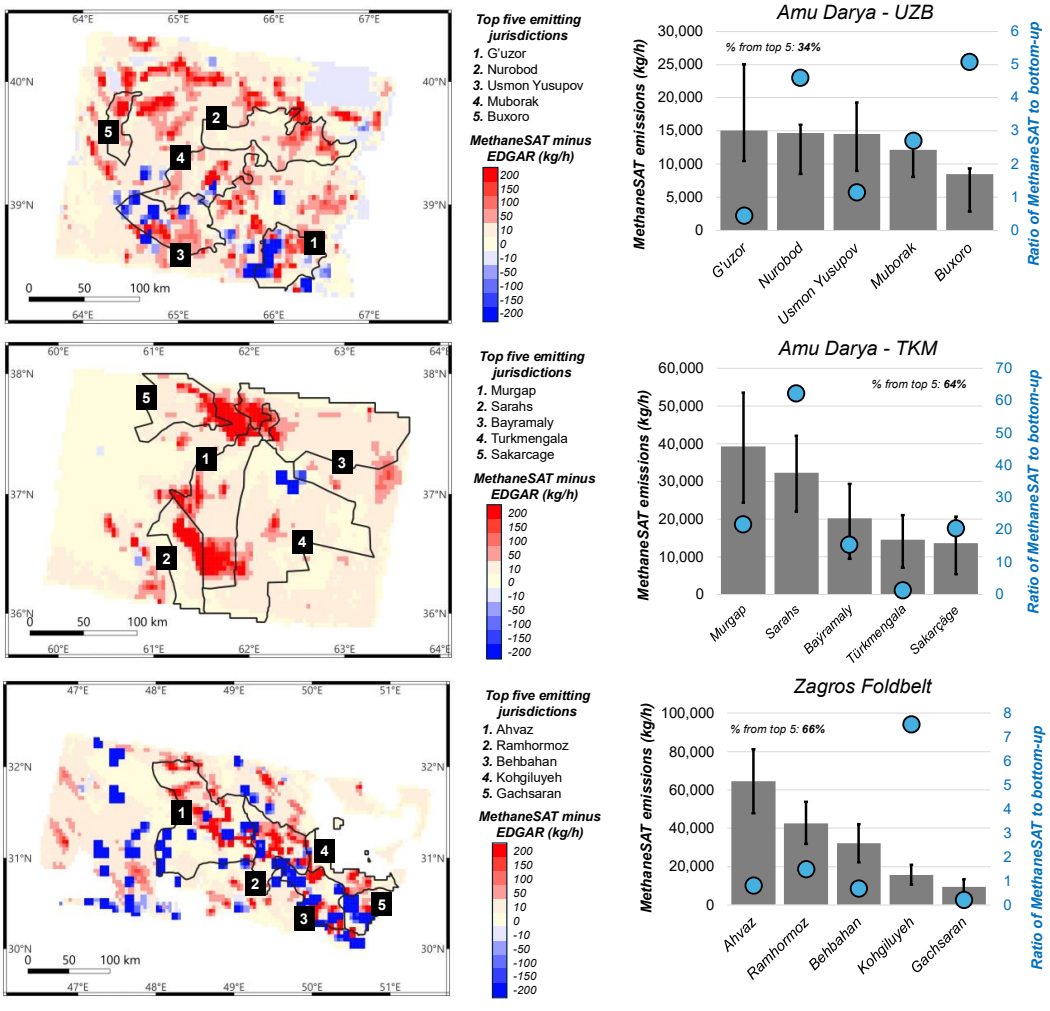

Fig. 6: Left column displays maps of the differences between MethaneSAT emissions estimates and the EDGAR_2025_GHG bottom-up methane inventory across jurisdictions (i.e., counties, districts). Right column displays the jurisdictions with the five highest MethaneSAT emissions estimates and the respective ratios compared to bottom-up inventories (i.e., MethaneSAT divided by the EDGAR_2025_GHG). The percentage of total emissions accounted for by the top five emitting counties/districts are indicated above each respective barplot.

https://doi.org/10.5194/egusphere-2025-6126
Preprint. Discussion started: 30 December 2025

4 Discussion

We provide new satellite-based quantification of methane emissions across six major oil and gas producing regions derived using MethaneSAT's high precision, high-resolution observations combined with its wide mapping domains (~220 km - 440 km swaths). Satellite observations offer measurement-based constraints that complement bottom-up inventories, reveal spatial emission patterns and potential new hot spots, and support targeted mitigation strategies[1,5,19]. Relative to previously published satellite-based estimates and existing bottom-up inventories, our analysis indicates consistently higher emissions in the Amu Darya – TKM region (Fig. 3; Fig. 4; Fig. 6). We estimate total methane emissions of 188 t/h in this basin, exceeding those reported for other major emitting regions such as the Haynesville-Bossier (US)[59] or even national-scale estimates for Saudi Arabia[14]. More specifically in the region, we observe consistent and elevated underestimation by bottom-up inventories in Sarahs District and over the city of Mary, which is further supported by co-located methane hotspots detected from TROPOMI. These results not only underscore the importance of updated, measurement-based assessments for the Amu Darya basin in Turkmenistan, but the value of high-resolution methane emissions maps that can highlight specific jurisdictions responsible for the underestimation of methane emissions in bottom-up inventories, which are important for accounting and mitigation of methane emissions.

Oil and gas intensity metrics, both normalized by marketed gas production (i.e., loss rates) and combined energy production, function as a performance standard for oil and gas operators and highlight the cost-effectiveness of mitigation from the oil and gas sector[45]. We find elevated loss rates in both the San Joaquin and Zagros Foldbelt basins relative to the other regions we analyzed in this work. Both the San Joaquin and Zagros Foldbelt basins are primarily oil-producing and characterized by a long legacy of oil and gas development, with aging and potentially inefficient infrastructure that may be leading to the high loss rates. In contrast, the Eagle Ford basin has the lowest loss rate and is the youngest oil and gas basin among the basins we cover. All of the oil and gas basins studied in this work have loss rates well above the 0.20% methane intensity target set by the oil and gas decarbonization charter to reduce industry's emissions by year 2030[44], noting that operators within Turkmenistan, Uzbekistan, and Iran are not participants in this coalition. At a finer-scale than basin-wide estimates, the high-resolution methane emissions heatmaps from MethaneSAT highlighted significant interstate differences in the Permian basin with loss rates observed across the New Mexico and Texas state boundaries of the Delaware subbasin at 1.3% and 3.1% respectively, a finding also observed in TROPOMI-based inversions from 2019-2023[58]. These findings of lower loss rates in the New Mexico portion of the Delaware sub-basin of Permian coincide with stronger emission controls introduced in New Mexico relative to Texas[75]. While beyond the scope of this work and subject to associated uncertainties, MethaneSAT emissions maps can be used to derive methane intensities across individual jurisdictions, although a key limiting factor would be the granularity of oil and gas production data, especially for regions outside of the US. Even in the US, the heterogeneity and comingling of oil and gas operators prevents specific operator attribution from MethaneSAT observations, except for point source detections[23] which are not included in this work as the focus of this study is on regional and sub-regional emissions. Internationally, many countries are dominated by state-owned oil and gas operations where attribution to oil and gas producers is more straightforward.

https://doi.org/10.5194/egusphere-2025-6126
Preprint. Discussion started: 30 December 2025

Nevertheless, these results demonstrate basin, sub-basin and individual jurisdictional-scale emission insights derived using the relatively short operational lifetime of MethaneSAT towards advancing the state of emission quantification in order to further support and motivate methane mitigation action from the oil and gas sector.

We investigate emissions estimates at county/district-level scales to identify the highest emitting subregions and localize areas of discrepancies compared to bottom-up inventories. Importantly, bottom-up inventories and methane emissions data from MethaneSAT differ in their temporal representation (i.e., annual estimates versus an aggregation of multiple satellite overpasses). However, we can infer insights into the spatial distribution of emissions across jurisdictions and identify subregions where inventories potentially under- or over-estimate emissions. In the US, we compare MethaneSAT emissions estimates to 2020 annual estimates from the EPA-GHGI and find consistent underestimation in the national inventory across multiple counties/districts (Fig. 5), with the highest emissions in Reeves County (US, Texas) at 49 t/h which are a factor of ~10 higher than the EPA-GHGI. We also find, in the Permian basin, that counties in New Mexico have more comparable emissions to the EPA-GHGI compared to those in Texas. Discrepancies between bottom-up estimates and top-down inversions are consistently observed in the US[11,21,59], further supporting refinements to bottom-up emissions estimates where agreement between bottom-up and top-down can improve[27,47]. There are several examples of refined bottom-up inventories in the US, including the VISTA-CA[76] dairy emissions inventory in the San Joaquin region where Schulze et al.[77] found greater agreement compared to independent mass-balance flights, or the EI-ME oil and gas emissions inventory presented in Omara et al.[39] where national oil and gas emissions estimates were in wide agreement with multiple satellite-based estimates. Outside of the US, we observe the highest emissions in Ahvaz District (Iran) at 82 t/h, but find comparable emissions estimates to EDGAR (Fig. 4, Fig. 6). Other broader insights include the relative contribution of emissions from jurisdictionally boundaries to larger regional estimates. For example, in the Permian and Amu Darya - UZB regions, the contribution from the top five districts/counties (ie., 41% and 34% respectively) indicate a greater spread of emissions across the entire measurement domains. In the San Joaquin, Zagros Foldbelt, and Amu Darya - TKM regions we find higher contributions from the top five emitting jurisdictions at 84%, 66%, and 64% respectively, which indicates that emissions are more localized. A key factor to consider when quantifying emissions for these smaller regions is the growth in uncertainty as the spatial domain of interest becomes smaller [78]. In the context of MethaneSAT, this effect is most pronounced when analyzing emissions from single 0.04° × 0.04° emission rate estimates (i.e., a single grid cell). Repeated observations can help reduce this uncertainty and identify more robust trends over space and time, but conclusions derived from a single observation grid from MethaneSAT should be subject to large uncertainty. Emission estimates for larger subregions with multiple observations will inherently be more robust due to the aggregation of data and partial cancellation of random errors, increasing the statistical confidence in any conclusions derived from the data.

MethaneSAT does not incorporate a bottom-up prior emissions inventory to inform the spatial allocation of methane emissions and therefore it relies on the high-precision measurement aspects of the input XCH4 data which resolves methane concentration gradients at high precision (2.5 – 5.5 ppb at 2 km x 2 km resolution)[79]. In the post analysis of MethaneSAT data, we utilize a composite prior emissions inventory for the sectoral allocation of methane emissions

https://doi.org/10.5194/egusphere-2025-6126
Preprint. Discussion started: 30 December 2025

based on sector-specific estimates from multiple spatially explicit datasets [3,4,36,37,47] including global point source data from Carbon Mapper[40] to create a more comprehensive and spatially resolved dataset. We use this approach to improve the sectoral allocation of methane emissions by sector after the flux inversion process, especially for regions where information on oil and gas emissions data is sparse and information from one inventory can account for discrepancies in another (Fig. S5). An additional characteristic from sectoral emissions estimates from MethaneSAT, are relatively high methane emissions associated with non-oil and gas emissions compared to other spatially-explicit inventories (Fig. 3) which we also observe in other satellite-based datasets such as Varon et al.[58] in our Permian methane emissions estimates. Most of our sectoral-attributed non-oil and gas emission estimates from MethaneSAT originate from agricultural sources (Fig. 3), which reflects agricultural emissions within prior inventories that cover much larger areas than the localized oil and gas emissions within the same inventories. Artifacts from the MethaneSAT inversion process arising from wind errors coupled with a non-negativity of emissions quantification may be expected to result in small contributions (i.e., <15%) of diffuse emissions throughout the scenes, which are predominantly allocated to agricultural sources in the absence of others.

5 Conclusions

The results we present here are a summary of insights from six diverse oil and gas producing regions around the world, with any single region deserving of more focused analysis. Among our results, the statistically robust methane emissions quantifications across jurisdictional bounds is perhaps the most influential for supporting countries/industries/cities to monitor and mitigate methane emissions. Fine-scale methane emissions data illuminates specific areas of discrepancies from bottom-up inventories which are commonly used to inform methane mitigation policy – all through atmospheric observations. A key example we show is found in the Amu Darya region of Turkmenistan, where further investigation could shed more light to the specific sectors and sources of the large discrepancies we find. Other broader insights include the consistent discrepancy with the EPA-GHGI , as well as gas-production normalized loss rates exceeding 10% in the oil-dominant basins of San Joaquin and Zagros Foldbelt which are both characterized by legacy oil and gas producing infrastructure. Many capabilities of MethaneSAT are demonstrated in this work, and future improvements to data acquired and processed over the lifetime of the satellite will continue to be refined and released in the public domain to help further improve the understanding and mitigation potential of methane emissions at multiple scales in particular across the oil and gas sector.

https://doi.org/10.5194/egusphere-2025-6126
Preprint. Discussion started: 30 December 2025

Appendix A: Description of MethaneSAT emissions inversion process

Methane emissions inversions from MethaneSAT data produce 0.04° x 0.04° (i.e., 4 x 4 km^2) resolution methane emission maps of total methane emissions at spatial scales of roughly 220 x 440 km^2 from a single overpass (i.e., a "collection"). The satellite is equipped with a pair of Littrow passive imaging spectrometers that measure the column-averaged dry-air mole fraction of methane (i.e., XCH4) at a resolution of ~110 m x 400 m at nadir with a precision of 2.5- 5.5 ppb at 2 x 2 km^2 [79]. The inverse modelling system for MethaneSAT intakes XCH4 observations, meteorological data from the Global Forecast System (NOAA, 2015-present), a model of the topographic variation in background XCH4, and an uninformative lognormal prior as inputs to the inversion process. Using the Stochastic Time-Inverted Lagrangian Transport (STILT)[80,81] model, we calculate a Jacobian function that links XCH4 enhancements to upwind sources and use the Stan software package[82] to optimize the emissions and the background concentration using the No-U-Turn Sampler (NUTS)[83].

MethaneSAT observations yield methane concentration fields that exhibit variability on different spatial scales. This variability is caused by either (a) topography in the observed region, (b) variability in the boundary inflow (i.e., the air flowing into the observed region from upwind), and (c) enhancements caused by surface fluxes within the observed region. We account for the topographic effect in the background concentration induced by a combination of the vertical atmospheric profile of methane concentration and the averaging kernel of the satellite measurement[84] (ie., the MethaneSAT XCH4 retrieval prior) which relies on the Total Carbon Column Observing Network GGG 2020 model[85]. The boundary inflow is a combination of the background concentration of methane and the inflow variability, the latter resulting from upwind sources and mesoscale concentration gradients. We optimize those components alongside the surface fluxes inside the observed region, using STILT model footprints to link flux rates to predicted concentration enhancements. We only report fluxes inside the observed region ("interior domain"), since those are well informed by our observations.

The MethaneSAT inverse modelling process estimates XCH4 (z) as a sum of contributions from emissions (Hs) and a field of background concentration (z_b), where H is a Jacobian matrix linking variations in methane concentrations to emissions where each row corresponds to an XCH4 observation and each column corresponds to emissions at a location in space. We decompose the contributions from emissions into those from the interior domain ($H_{interior}s_{interior}$), and the contributions from the domain upwind of the interior domain (the "exterior domain", $H_{exterior}s_{exterior}$). We decompose the field of background concentrations into the contributions from topographical variations (z_{topo}) and a slowly varying background (z_{bg}).

$$z = Hs + z_b = H_{interior}s_{interior} + H_{exterior}s_{exterior} + z_{topo} + z_{bg}$$

Observations are aggregated to a resolution of 2 km x 2 km where any grid cell containing less than 50% valid data is discarded. The model optimizes the interior fluxes on a 4 km x 4 km grid, while the observations are aggregated to 2 km x 2 km. Exterior emitters are clustered in 350 similar areas with the KMEANS algorithm[86] based on the cosine-distance between their Jacobian footprint which reduces co-linearity between model parameters while

https://doi.org/10.5194/egusphere-2025-6126
Preprint. Discussion started: 30 December 2025

preserving the expressivity of the boundary inflow model. STILT footprints extend 28 hours back in time from the satellite observation, which is the ventilation time scale for the observed region size in typical wind conditions, while assuming constant emissions during this time. This means that individual MethaneSAT emissions maps represent emissions over a duration of 28 hours, which partially addresses any variations impacted by diurnal emissions patterns in our overall estimates[27].

Appendix B: Uncertainty calculations

Uncertainty in the MethaneSAT emissions product is dominated by: 1) uncertainty in the meteorological product used to generate the STILT Jacobian that links emissions with concentrations, 2) correlated uncertainty in the observations (e.g., striping), 3) uncertainty in the background concentration, 4) uncertainty in the allocation of signal between emissions in the reported domain and the boundary inflow, and 5) uncertainty in the emission map as expressed by the variability in samples in a Markov Chain Monte Carlo (MCMC) simulation. We use a bootstrap resampling of the MCMC samples to estimate uncertainty for methane emissions for each emissions map, with propagation of uncertainty from each of the above effects by either sweeping across values of input parameters (e.g., recomputing the inversions with high and low estimates of the mean background concentration) or modifying each sample (e.g., errors in the wind speed data). Uncertainty on the total dispersed area emissions is the 95% confidence interval on the total across all samples (n=4,000), with an additional 20% uncertainty added to account for assumed uncertainty in the static parameters in the input GFS weather data used for the inversions.

We calculate uncertainties in the aggregated regional-level estimates by stacking the results of the 4,000 samples from the MCMC simulations for each emissions cell. Where multiple emissions maps find emissions for the same cell, then we randomly resample from these emissions maps and average cell-level emissions estimates across layers to obtain 4,000 estimates of an aggregated mean value representing the estimated methane emissions within that subregion. We perform this sub-regional averaging and aggregation across all areas with unique combinations of emissions maps (Fig. 1). We then add all total methane estimates for each subregion across all 4,000 samples to calculate the 97.5^{th} and 2.5^{th} percentiles of the total methane emissions of the entire aggregated spatial domain.

To calculate uncertainties related to the disaggregation of methane emissions by sector, we bootstrap with resampling the input data used to create the prior emissions estimates in our stacked prior inventory, which are in turn used to re-calculate the disaggregation of methane emissions (n=4,000). For the bottom-up inventories, regardless of the sector, we assume a normal distribution with a standard deviation of 50% for the cell-level emissions estimates. For the point sources from Carbon Mapper, we use the provided source-level standard deviations assuming a normal distribution to resample the emission rates (n=4,000). Sectoral ratios of methane emissions are then calculated 4,000 times using these resampled input data to provide upper and lower bounds on the uncertainty for the associated sectoral methane emissions, which we then use to obtain the 97.5^{th} and 2.5^{th} percentiles as the associated uncertainty. To calculate the final uncertainty on the sectoral disaggregation of methane emissions, we combine the uncertainty on the total methane emissions estimates with the sectoral uncertainties and

https://doi.org/10.5194/egusphere-2025-6126
Preprint. Discussion started: 30 December 2025

an additional uncertainty relating to the percentage of unknown methane emissions to the total. Notably, this additional uncertainty relating to the unknown attribution of methane emissions from MethaneSAT contributes only <1% of uncertainty to the total for the regions we analyze in this work.

Data availability: Composite emissions maps are available for download at Zenodo (link: xxxx), with associated links to the individual MethaneSAT scenes listed and publicly available through Google Earth Engine, and data used to reproduce the figures in the main text. Code used to produce emission map aggregation and sectoral disaggregation are available upon reasonable request.

Supplement: The supplement to this preprint is available online.

Author contribution: JPW and RG conceived the study. Funding acquisition was led by RG, SCW, and SPH. Data collection and field measurements were conducted by JPW, JB, MK, MO, AH, KW, BL, JW, and KM. Data processing and software development were performed by EK, JB, MK, SA, MR, NL, TM, CCM, SR, MS, JF, BL, and DM. Formal data analysis was carried out by JPW, MO, AH, KW, BL, MK, and JB. Visualization and figure preparation were led by JPW, with contributions from MO, AH, KW, and BL. Methodology development was conducted by JPW, JB, MK, SA, MR, NL, TM, CCM, and SR. Project supervision was provided by RG. JPW wrote the original draft of the manuscript. Writing, review, and editing were contributed by RG, MO, EK, DM, MK, KM, and LG.

Financial support: Funding for MethaneSAT activities was provided in part by anonymous donors, Arnold Ventures, The Audacious Project, the Ballmer Group, the Bezos Earth Fund, The Children's Investment Fund Foundation, the Heising–Simons Family Fund, King Philanthropies, the Robertson Foundation, the Skyline Foundation, and the Valhalla Foundation. For a more complete list of funders, please visit https://www.methanesat.org/ (last access: 8 December 2025).

Competing interests: The authors report no competing interests.

https://doi.org/10.5194/egusphere-2025-6126
Preprint. Discussion started: 30 December 2025

4. References

1. Saunois, M. *et al.* Global Methane Budget 2000–2020. *Earth System Science Data* **17**, 1873–1958 (2025).
2. Nisbet, E. G. *et al.* Methane Mitigation: Methods to Reduce Emissions, on the Path to the Paris Agreement. *Reviews of Geophysics* **58**, e2019RG000675 (2020).
3. Maasakkers, J. D. *et al.* A Gridded Inventory of Annual 2012–2018 U.S. Anthropogenic Methane Emissions. *Environ. Sci. Technol.* **57**, 16276–16288 (2023).
4. Crippa, M. *et al.* Insights into the spatial distribution of global, national, and subnational greenhouse gas emissions in the Emissions Database for Global Atmospheric Research (EDGAR v8.0). *Earth System Science Data* **16**, 2811–2830 (2024).
5. Jacob, D. J. *et al.* Quantifying methane emissions from the global scale down to point sources using satellite observations of atmospheric methane. *Atmospheric Chemistry and Physics* **22**, 9617–9646 (2022).
6. Jervis, D. *et al.* The GHGSat-D imaging spectrometer. *Atmospheric Measurement Techniques* **14**, 2127–2140 (2021).
7. Duren, R. *et al.* The Carbon Mapper emissions monitoring system. *EGUsphere* 1–41 (2025) doi:10.5194/egusphere-2025-2275.
8. Warren, J. D. *et al.* Sectoral contributions of high-emitting methane point sources from major U.S. onshore oil and gas producing basins using airborne measurements from MethaneAIR. *EGUsphere* 1–22 (2024) doi:10.5194/egusphere-2024-3865.
9. Lu, X. *et al.* Methane emissions in the United States, Canada, and Mexico: evaluation of national methane emission inventories and 2010–2017 sectoral trends by inverse analysis of in situ (GLOBALVIEWplus CH_4 ObsPack) and satellite (GOSAT) atmospheric observations. *Atmospheric Chemistry and Physics* **22**, 395–418 (2022).
10. Nesser, H. *et al.* High-resolution US methane emissions inferred from an inversion of 2019 TROPOMI satellite data: contributions from individual states, urban areas, and landfills. *Atmospheric Chemistry and Physics* **24**, 5069–5091 (2024).
11. Shen, L. *et al.* Satellite quantification of oil and natural gas methane emissions in the US and Canada including contributions from individual basins. *Atmospheric Chemistry and Physics* **22**, 11203–11215 (2022).
12. Guanter, L. *et al.* Surveying Methane Point-Source Super-Emissions across Oil and Gas Basins with MethaneSAT. *EGUsphere* 1–29 (2025) doi:10.5194/egusphere-2025-4666.
13. Lu, X. *et al.* Global methane budget and trend, 2010–2017: complementarity of inverse analyses using in situ (GLOBALVIEWplus CH_4 ObsPack) and satellite (GOSAT) observations. *Atmospheric Chemistry and Physics* **21**, 4637–4657 (2021).
14. Worden, J. R. *et al.* The 2019 methane budget and uncertainties at 1° resolution and each country through Bayesian integration Of GOSAT total column methane data and a priori inventory estimates. *Atmospheric Chemistry and Physics* **22**, 6811–6841 (2022).

https://doi.org/10.5194/egusphere-2025-6126
Preprint. Discussion started: 30 December 2025

15. Qu, Z. *et al.* Global distribution of methane emissions: a comparative inverse analysis of observations from the TROPOMI and GOSAT satellite instruments. *Atmospheric Chemistry and Physics* **21**, 14159–14175 (2021).
16. Varon, D. J. *et al.* Continuous weekly monitoring of methane emissions from the Permian Basin by inversion of TROPOMI satellite observations. *Atmospheric Chemistry and Physics* **23**, 7503–7520 (2023).
17. Chen, Z. *et al.* Satellite quantification of methane emissions and oil–gas methane intensities from individual countries in the Middle East and North Africa: implications for climate action. *Atmospheric Chemistry and Physics* **23**, 5945–5967 (2023).
18. Veefkind, J. P. *et al.* Widespread Frequent Methane Emissions From the Oil and Gas Industry in the Permian Basin. *Journal of Geophysical Research: Atmospheres* **128**, e2022JD037479 (2023).
19. Shen, L. *et al.* National quantifications of methane emissions from fuel exploitation using high resolution inversions of satellite observations. *Nat Commun* **14**, 4948 (2023).
20. Lu, X. *et al.* Observation-derived 2010-2019 trends in methane emissions and intensities from US oil and gas fields tied to activity metrics. *Proceedings of the National Academy of Sciences* **120**, e2217900120 (2023).
21. Alvarez, R. A. *et al.* Assessment of methane emissions from the U.S. oil and gas supply chain. *Science* **361**, 186–188 (2018).
22. Schuit, B. J. *et al.* Automated detection and monitoring of methane super-emitters using satellite data. *Atmospheric Chemistry and Physics* **23**, 9071–9098 (2023).
23. Guanter, L. *et al.* Surveying Methane Point-Source Super-Emissions across Oil and Gas Basins with MethaneSAT. *EGUsphere* 1–29 (2025) doi:10.5194/egusphere-2025-4666.
24. Scanlon, B. R., Reedy, R. C., Male, F. & Walsh, M. Water Issues Related to Transitioning from Conventional to Unconventional Oil Production in the Permian Basin. *Environ. Sci. Technol.* **51**, 10903–10912 (2017).
25. Duren, R. M. *et al.* California's methane super-emitters. *Nature* **575**, 180–184 (2019).
26. Miller, D. J. *et al.* Ammonia and methane dairy emission plumes in the San Joaquin Valley of California from individual feedlot to regional scales. *Journal of Geophysical Research: Atmospheres* **120**, 9718–9738 (2015).
27. Vechi, N. T., Mellqvist, J., Samuelsson, J., Offerle, B. & Scheutz, C. Ammonia and methane emissions from dairy concentrated animal feeding operations in California, using mobile optical remote sensing. *Atmospheric Environment* **293**, 119448 (2023).
28. California - San Joaquin Basin Onshore Crude Oil Estimated Production from Reserves (Million Barrels). https://www.eia.gov/dnav/pet/hist/LeafHandler.ashx?n=PET&s=RCRR10RCAJ_1&f=A.
29. California Natural Gas Gross Withdrawals (Million Cubic Feet). https://www.eia.gov/dnav/ng/hist/n9010ca2m.htm.
30. Dávila-Pulido, G. I., González-Ibarra, A. A. & Garza-García, M. A brief review on coal reserves, production and possible non-power uses: The case of Mexico. *Heliyon* **9**, (2023).

https://doi.org/10.5194/egusphere-2025-6126
Preprint. Discussion started: 30 December 2025

31. Eagle Ford natural gas production increases as crude oil production holds steady - U.S. Energy Information Administration (EIA). https://www.eia.gov/todayinenergy/detail.php?id=64984.
32. Lens: Natural Resources Data Analytics Platform. https://www.woodmac.com/lens (2021).
33. Yu, Y. *et al.* Division and resources evaluation of hydrocarbon plays in the Amu Darya basin, central Asia. *Petroleum Exploration and Development* **42**, 819–826 (2015).
34. Ulmishek, G. F. *Petroleum Geology and Resources of the Amu-Darya Basin, Turkmenistan, Uzbekistan, Afghanistan, and Iran*. vol. 2201 (US Department of the Interior, US Geological Survey Iran, 2004).
35. Alipour, M. Petroleum systems of the Iranian Zagros Fold and Thrust Belt. *Results in Earth Sciences* **2**, 100027 (2024).
36. Granier, C. *et al. The Copernicus Atmosphere Monitoring Service Global and Regional Emissions (April 2019 Version)*. https://hal.science/hal-02322431 (2019) doi:10.24380/d0bn-kx16.
37. Scarpelli, T. R. *et al.* Updated Global Fuel Exploitation Inventory (GFEI) for methane emissions from the oil, gas, and coal sectors: evaluation with inversions of atmospheric methane observations. *Atmospheric Chemistry and Physics* **22**, 3235–3249 (2022).
38. Cusworth, D. H. *et al.* A Bayesian framework for deriving sector-based methane emissions from top-down fluxes. *Commun Earth Environ* **2**, 242 (2021).
39. Omara, M. *et al.* Constructing a measurement-based spatially explicit inventory of US oil and gas methane emissions. *Earth System Science Data Discussions* 1–25 (2024) doi:10.5194/essd-2024-72.
40. Dashboard | Carbon Mapper. https://data.carbonmapper.org/#1.3/30.8/50.5.
41. CMS: Global 0.5-deg Wetland Methane Emissions and Uncertainty (WetCHARTs v1.3.3) - NASA Open Data Portal. https://data.nasa.gov/dataset/cms-global-0-5-deg-wetland-methane-emissions-and-uncertainty-wetcharts-v1-3-3-d9498.
42. Fung, I. *et al.* Three-dimensional model synthesis of the global methane cycle. *Journal of Geophysical Research: Atmospheres* **96**, 13033–13065 (1991).
43. OGDC - The Charter. *OGDC* https://www.ogdc.org/.
44. Oil and Gas Climate Initiative | OGCI. https://www.ogci.com/.
45. Overview – Global Methane Tracker 2022 – Analysis. *IEA* http://www.iea.org/reports/global-methane-tracker-2022/overview.
46. N.M. Code R. § 19.15.27.9 Statewide Natural Gas Capture Requirements. *vLex* https://regulations.vlex.com/vid/n-m-code-r-955851862.
47. Omara, M. *et al.* Developing a spatially explicit global oil and gas infrastructure database for characterizing methane emission sources at high resolution. *Earth System Science Data* **15**, 3761–3790 (2023).

https://doi.org/10.5194/egusphere-2025-6126
Preprint. Discussion started: 30 December 2025

48. Robertson, A. M. *et al.* New Mexico Permian Basin Measured Well Pad Methane Emissions Are a Factor of 5–9 Times Higher Than U.S. EPA Estimates. *Environ. Sci. Technol.* **54**, 13926–13934 (2020).
49. Yu, J. *et al.* Methane Emissions from Natural Gas Gathering Pipelines in the Permian Basin. *Environ. Sci. Technol. Lett.* **9**, 969–974 (2022).
50. PermianMAP. https://data.permianmap.org/pages/operators.
51. Barkley, Z. *et al.* Quantification of oil and gas methane emissions in the Delaware and Marcellus basins using a network of continuous tower-based measurements. *Atmospheric Chemistry and Physics* **23**, 6127–6144 (2023).
52. Chen, Y. *et al.* Quantifying Regional Methane Emissions in the New Mexico Permian Basin with a Comprehensive Aerial Survey. *Environ. Sci. Technol.* **56**, 4317–4323 (2022).
53. Cusworth, D. H. *et al.* Intermittency of Large Methane Emitters in the Permian Basin. *Environ. Sci. Technol. Lett.* **8**, 567–573 (2021).
54. Hmiel, B. *et al.* Empirical quantification of methane emission intensity from oil and gas producers in the Permian basin. *Environ. Res. Lett.* **18**, 024029 (2023).
55. Sherwin, E. D. *et al.* US oil and gas system emissions from nearly one million aerial site measurements. *Nature* **627**, 328–334 (2024).
56. Cusworth, D. H. *et al.* Strong methane point sources contribute a disproportionate fraction of total emissions across multiple basins in the United States. *Proceedings of the National Academy of Sciences* **119**, e2202338119 (2022).
57. Irakulis-Loitxate, I. *et al.* Satellite-based survey of extreme methane emissions in the Permian basin. *Science Advances* **7**, eabf4507 (2021).
58. Varon, D. J. *et al.* Seasonality and declining intensity of methane emissions from the Permian and nearby US oil and gas basins. https://eartharxiv.org/repository/view/9533/ (2025).
59. MacKay, K. *et al.* Assessment of methane emissions from US onshore oil and gas production using MethaneAIR measurements. *EGUsphere* 1–24 (2025) doi:10.5194/egusphere-2025-3008.
60. Omara, M. *et al.* Methane Emissions from Natural Gas Production Sites in the United States: Data Synthesis and National Estimate. *Environ. Sci. Technol.* **52**, 12915–12925 (2018).
61. Omara, M. *et al.* Methane emissions from US low production oil and natural gas well sites. *Nat Commun* **13**, 2085 (2022).
62. Cui, Y. Y. *et al.* Top-down estimate of methane emissions in California using a mesoscale inverse modeling technique: The San Joaquin Valley. *Journal of Geophysical Research: Atmospheres* **122**, 3686–3699 (2017).
63. Barrowman, S., Yurco, K., Sumner, D. & Cooper, M. H. MORE MILK, FEWER FARMS, and REGIONAL CONCENTRATION: MAPPING TRANSFORMATIONS IN CALIFORNIA'S DAIRY INDUSTRY. *Geographical Review* **115**, 49–80 (2025).

https://doi.org/10.5194/egusphere-2025-6126
Preprint. Discussion started: 30 December 2025

64. Uzbekistan - Countries & Regions. *IEA* https://www.iea.org/countries/uzbekistan/oil.
65. Western, L. M. *et al.* Estimates of North African Methane Emissions from 2010 to 2017 Using GOSAT Observations. *Environ. Sci. Technol. Lett.* **8**, 626–632 (2021).
66. Chen, Z. *et al.* Satellite quantification of methane emissions and oil–gas methane intensities from individual countries in the Middle East and North Africa: implications for climate action. *Atmospheric Chemistry and Physics* **23**, 5945–5967 (2023).
67. Greenhouse Gas Inventory Data - Detailed data by Party. https://di.unfccc.int/detailed_data_by_party.
68. Varon, D. J. *et al.* Satellite Discovery of Anomalously Large Methane Point Sources From Oil/Gas Production. *Geophysical Research Letters* **46**, 13507–13516 (2019).
69. Varon, D. J. *et al.* High-frequency monitoring of anomalous methane point sources with multispectral Sentinel-2 satellite observations. *Atmospheric Measurement Techniques* **14**, 2771–2785 (2021).
70. Satellites Detect Abatable Super-Emissions in One of the World's Largest Methane Hotspot Regions | Environmental Science & Technology. https://pubs.acs.org/doi/full/10.1021/acs.est.1c04873.
71. Iraq - Countries & Regions. *IEA* https://www.iea.org/countries/iraq.
72. Iran - Countries & Regions. *IEA* https://www.iea.org/countries/iran.
73. Batista Cruz, R. Y. *et al.* Water reservoirs in open coal pits: A useful resource for NE of Mexico? *Journal of South American Earth Sciences* **165**, 105731 (2025).
74. Heerah, S. *et al.* Dairy Methane Emissions in California's San Joaquin Valley Inferred With Ground-Based Remote Sensing Observations in the Summer and Winter. *Journal of Geophysical Research: Atmospheres* **126**, e2021JD034785 (2021).
75. MethaneSAT observations reveal lower methane intensity in New Mexico's Permian Basin associated with emissions control. https://www.edf.org/methanesat-observations-reveal-lower-methane-intensity-new-mexicos-permian-basin-associated.
76. Marklein, A. R. *et al.* Facility-scale inventory of dairy methane emissions in California: implications for mitigation. *Earth System Science Data* **13**, 1151–1166 (2021).
77. Schulze, B. C. *et al.* Methane Emissions from Dairy Operations in California's San Joaquin Valley Evaluated Using Airborne Flux Measurements. *Environ. Sci. Technol.* **57**, 19519–19531 (2023).
78. Heuvelink, G. B. M. *Error Propagation in Environmental Modelling with GIS*. (CRC Press, London, 1998). doi:10.4324/9780203016114.
79. Chan Miller, C. *et al.* Methane retrieval from MethaneAIR using the CO_2 proxy approach: a demonstration for the upcoming MethaneSAT mission. *Atmospheric Measurement Techniques* **17**, 5429–5454 (2024).

https://doi.org/10.5194/egusphere-2025-6126
Preprint. Discussion started: 30 December 2025

80. A near-field tool for simulating the upstream influence of atmospheric observations: The Stochastic Time-Inverted Lagrangian Transport (STILT) model - Lin - 2003 - Journal of Geophysical Research: Atmospheres - Wiley Online Library. https://agupubs.onlinelibrary.wiley.com/doi/full/10.1029/2002JD003161.

81. Fasoli, B., Lin, J. C., Bowling, D. R., Mitchell, L. & Mendoza, D. Simulating atmospheric tracer concentrations for spatially distributed receptors: updates to the Stochastic Time-Inverted Lagrangian Transport model's R interface (STILT-R version 2). *Geoscientific Model Development* **11**, 2813–2824 (2018).

82. Carpenter, B. *et al.* Stan: A Probabilistic Programming Language. *Journal of Statistical Software* **76**, 1–32 (2017).

83. Hoffman, M. D. & Gelman, A. The No-U-Turn sampler: adaptively setting path lengths in Hamiltonian Monte Carlo. *Journal of Machine Learning Research* https://www.jmlr.org/papers/volume15/hoffman14a/hoffman14a.pdf.

84. Borsdorff, T., Hasekamp, O. P., Wassmann, A. & Landgraf, J. Insights into Tikhonov regularization: application to trace gas column retrieval and the efficient calculation of total column averaging kernels. *Atmospheric Measurement Techniques* **7**, 523–535 (2014).

85. ESSD - The Total Carbon Column Observing Network's GGG2020 data version. https://essd.copernicus.org/articles/16/2197/2024/essd-16-2197-2024.html.

86. Ester, M., Kriegel, H.-P., Sander, J. & Xu, X. A density-based algorithm for discovering clusters in large spatial databases with noise. *KDD-96 Proceedings* https://cdn.aaai.org/KDD/1996/KDD96-037.pdf?source=post_page----------.